Numerical Treatment of the Filament-Based Lamellipodium Model (FBLM)

Angelika Manhart, Dietmar Oelz, Christian Schmeiser and Nikolaos Sfakianakis

Abstract We describe in this work the numerical treatment of the Filament-Based Lamellipodium Model (FBLM). This model is a two-phase two-dimensional continuum model, describing the dynamics of two interacting families of locally parallel F-actin filaments. It includes, among others, the bending stiffness of the filaments, adhesion to the substrate, and the cross-links connecting the two families. The numerical method proposed is a Finite Element Method (FEM) developed specifically for the needs of this problem. It is comprised of composite Lagrange–Hermite two-dimensional elements defined over a two-dimensional space. We present some elements of the FEM and emphasize in the numerical treatment of the more complex terms. We also present novel numerical simulations and compare to in-vitro experiments of moving cells.

1 Introduction

The lamellipodium is a flat cell protrusion functioning as a motility organelle in protrusive cell migration [28]. It is a very dynamic structure mainly consisting of a network of branched actin filaments. These are semi-elastic rods that represent the polymer form of the protein actin. They are continuously remodeled by polymeriza-

A. Manhart · C. Schmeiser
Faculty of Mathematics, University of Vienna, Oskar-Morgenstern Platz 1,
1090 Vienna, Austria
e-mail: angelika.manhart@univie.ac.at

C. Schmeiser
e-mail: christian.schmeiser@univie.ac.at

D. Oelz
Courant Institute of Mathematical Sciences, New York University,
251 Mercer Street, New York, NY 10012-1185, USA
e-mail: dietmar@cims.nyu.edu

N. Sfakianakis (✉)
Johannes-Gutenberg University, Staudungerweg 9, 55099 Mainz, Germany
e-mail: sfakiana@uni-mainz.de

tion and depolymerization and therefore undergo treadmilling [2]. Actin associated cross-linker proteins and myosin motor proteins integrate them into the lamellipodial meshwork which plays a key role in cell shape stabilization and in cell migration. Different modes of cell migration result from the interplay of protrusive forces due to polymerization, actomyosin dependent contractile forces and regulation of cell adhesion [9].

The first modeling attempts have resolved the interplay of protrusion at the front and retraction at the rear in a one-dimensional spatial setting [1, 6]. Two-dimensional continuum models were developed in order to include the lateral flow of F-actin along the leading edge of the cell into the quantitative picture. Those models can explain characteristic shapes of amoeboid cell migration [21, 22] on two-dimensional surfaces as well as the transition to mesenchymal migration [23].

One of the still unresolved scientific questions concerns the interplay between macroscopic observables of cell migration and the microstructure of the lamellipodium meshwork. Specialized models have been developed separately from the continuum approach to track microscopic information on filament directions and branching structure [8, 11, 24]. However, solving fluid-type models that describe the whole cytoplasm while retaining some information on the microstructure of the meshwork has turned out to be challenging. One approach is to formulate hybrid models [14], another one to directly formulate models on the computational, discrete level [13]. Recently the approach to directly formulate a computational model has been even extended into the three-dimensional setting making use of a finite element discretization [15].

In an attempt to create a simulation framework that addresses the interplay of macroscopic features of cell migration and the meshwork structure the Filament-Based Lamellipodium Model (FBLM) has been developed. It is a two-dimensional, two-phase, anisotropic continuum model for the dynamics of the lamellipodium network which retains key directional information on the filamentous substructure of this meshwork [20].

The model has been derived from a microscopic description based on the dynamics and interaction of individual filaments [18], and it has by recent extensions [12] reached a certain state of maturity. Since the model can be written in the form of a generalized gradient flow, numerical methods based on optimization techniques have been developed [19, 20]. Numerical efficiency had been a shortcoming of this approach. This has led to the development of a Finite Element numerical method which is presented in this article alongside simulations of a series of migration assays (Figs. 1 and 2).

2   Mathematical Modeling

In this section the FBLM will be sketched (see [12] for more detail). The main unknowns of the model are the positions of the actin filaments in two locally parallel families (denoted by the superscripts $+$ and $-$). Each of these families covers a
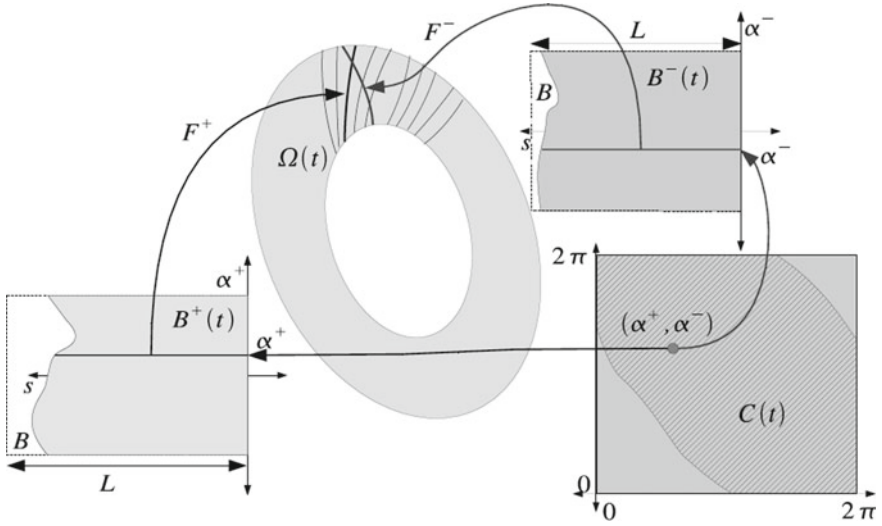
Fig. 1 Graphical representation of (3); showing here the lamellipodium $\Omega(t)$ "produced" by the mappings $\mathbf{F}^{\pm}$ and the crossing–filament domain $\mathscr{C}$
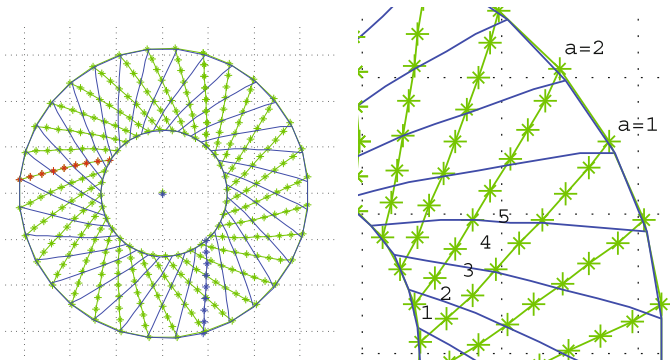

Fig. 2 Discretized lamellipodium (*left*) and lamellipodium fragment (*right*)

topological ring with all individual filaments connecting the inner boundary with the outer boundary. The outer boundaries are the physical leading edge and therefore identical, whereas the inner boundaries of the two families are artificial and may be different. Filaments are labeled by $\alpha \in [0, 2\pi)$, where the interval represents a one-dimensional torus, which means that in the following all functions of α are assumed periodic with period 2π. The maximal arclength of the filaments in an infinitesimal element $d\alpha$ of the $\pm$-family at time t is denoted by $L^{\pm}(\alpha, t)$, and an arclength parametrization of the filaments is denoted by $\{\mathbf{F}^{\pm}(\alpha, s, t) : -L^{\pm}(\alpha, t) \leq s \leq 0\} \subset \mathbb{R}^2$, where the leading edge corresponds to $s = 0$, i.e.

$$\left\{ \mathbf{F}^+(\alpha, 0, t) : 0 \le \alpha < 2\pi \right\} = \left\{ \mathbf{F}^-(\alpha, 0, t) : 0 \le \alpha < 2\pi \right\} \qquad \forall t , \qquad (1)$$

which together with

$$\left| \partial_s \mathbf{F}^\pm(\alpha, s, t) \right| = 1 \qquad \forall (\alpha, s, t) , \qquad (2)$$

constitutes constraints for the unknowns $\mathbf{F}^\pm$. The second constraint is connected to an *inextensibility* assumption on the filaments, which implies that s can also be interpreted as a monomer counter along filaments.

We expect that different filaments of the same family do not intersect each other, and each plus-filament crosses each minus-filament at most once. The first condition is guaranteed by $\det(\partial_\alpha \mathbf{F}^\pm, \partial_s \mathbf{F}^\pm) > 0$, where the sign indicates that the labeling with increasing α is in the clockwise direction. The second condition uniquely defines $s^\pm = s^\pm(\alpha^+, \alpha^-, t)$ such that $\mathbf{F}^+(\alpha^+, s^+, t) = \mathbf{F}^-(\alpha^-, s^-, t)$, for all $(\alpha^+, \alpha^-) \in \mathscr{C}(t)$, the set of all pairs of crossing filaments. It has to be noted that the validity of these properties is not guaranteed. For this and other reasons finite-time breakdown of the model cannot be excluded, although elements of the model like filament repulsion (see below) provides a regularization. As a consequence of the above assumptions, there are coordinate transformations $\psi^\pm : (\alpha^\mp, s^\mp) \mapsto (\alpha^\pm, s^\pm)$ such that

$$\mathbf{F}^\mp = \mathbf{F}^\pm \circ \psi^\pm .$$

In the following, we shall concentrate on one of the two families and skip the superscripts except that the other family is indicated by the superscript $*$. The heart of the FBLM is the force balance

$$0 = \underbrace{\mu^B \partial_s^2 \left(\eta \partial_s^2 \mathbf{F} \right)}_{\text{bending}} - \underbrace{\partial_s \left(\eta \lambda_{\text{inext}} \partial_s \mathbf{F} \right)}_{\text{inextensibility}} + \underbrace{\mu^A \eta D_t \mathbf{F}}_{\text{adhesion}} \qquad (3)$$

$$+ \underbrace{\partial_s \left(p(\rho) \partial_\alpha \mathbf{F}^\perp \right) - \partial_\alpha \left(p(\rho) \partial_s \mathbf{F}^\perp \right)}_{\text{pressure}}$$

$$\pm \underbrace{\partial_s \left(\eta \eta^* \widehat{\mu^T}(\phi - \phi_0) \partial_s \mathbf{F}^\perp \right)}_{\text{twisting}} + \underbrace{\eta \eta^* \widehat{\mu^S} \left(D_t \mathbf{F} - D_t^* \mathbf{F}^* \right)}_{\text{stretching}} ,$$

where the notation $\mathbf{F}^\perp = (F_1, F_2)^\perp = (-F_2, F_1)$ has been used. For fixed s and t, the function $\eta(\alpha, s, t)$, is the number density of filaments of length at least $-s$ at time t with respect to α. Its dynamics and that of the maximal length $L(\alpha, t)$ will not be discussed here. It can be modeled by incorporating the effects of polymerization, depolymerization, branching, and capping (see [12]). We only note that faster polymerization (even locally) leads to wider lamellipodia.

The first term on the right hand side of (3) describes the filaments' resistance against bending with the stiffness parameter $\mu^B > 0$. The second term is a tangential tension force, which arises from incorporating the inextensibility constraint (2) with the Lagrange multiplier $\lambda_{\text{inext}}(\alpha, s, t)$. The third term describes friction of

the filament network with the nonmoving substrate (see [18] for its derivation as a macroscopic limit of the dynamics of transient elastic adhesion linkages). Since filaments polymerize at the leading edge with the polymerization speed $v(\alpha, t) \geq 0$, they are continuously pushed into the cell with that speed, and the material derivative

$$D_t \mathbf{F} := \partial_t \mathbf{F} - v \partial_s \mathbf{F}$$

is the velocity of the actin material relative to the substrate. For the modeling of v see [12].

The second line of (3) models a pressure effect caused by Coulomb repulsion between neighboring filaments of the same family with pressure $p(\rho)$, where the actin density in physical space is given by

$$\rho = \frac{\eta}{|\det(\partial_\alpha \mathbf{F}, \partial_s \mathbf{F})|} \ . \tag{4}$$

Finally, the third line of (3) models the interaction between the two families caused by transient elastic cross-links and/or branch junctions. The first term describes elastic resistance against changing the angle $\phi = \arccos(\partial_s \mathbf{F} \cdot \partial_s \mathbf{F}^*)$ between filaments away from the angle ϕ_0 of the equilibrium conformation of the cross-linking molecule. The last term describes friction between the two families analogously to friction with the substrate. The friction coefficients have the form

$$\widehat{\mu^{T,S}} = \mu^{T,S} \left| \frac{\partial \alpha^*}{\partial s} \right| \ ,$$

with $\mu^{T,S} > 0$, and the partial derivative refers to the coordinate transformation ψ^*, which is also used when evaluating partial derivatives of $\mathbf{F}^*$.

The system (3) is considered subject to the boundary conditions

$$-\mu^B \partial_s \left(\eta \partial_s^2 \mathbf{F} \right) - p(\rho) \partial_\alpha \mathbf{F}^\perp + \eta \lambda_{\text{inext}} \partial_s \mathbf{F} \mp \eta \eta^* \widehat{\mu^T} (\phi - \phi_0) \partial_s \mathbf{F}^\perp \tag{5}$$

$$= \begin{cases} \eta \left(f_{\text{tan}}(\alpha) \partial_s \mathbf{F} + f_{\text{inn}}(\alpha) \mathbf{V}(\alpha) \right), & \text{for } s = -L \ , \\ \pm \lambda_{\text{tether}} \nu, & \text{for } s = 0 \ , \end{cases}$$

$$\eta \partial_s^2 \mathbf{F} = 0, \qquad \text{for } s = -L, 0 \ .$$

The terms in the second line are forces applied to the filament ends. The force in the direction ν orthogonal to the leading edge at $s = 0$ arises from the constraint (1) with the Lagrange parameter λ_{tether}. Its biological interpretation is due to tethering of the filament ends to the leading edge. The forces at the inner boundary $s = -L$ are models of the contraction effect of actin-myosin interaction in the interior region (see [12] for details).

3   Numerical Method

Before discretization, the problem for each filament family is transformed to a rectangular domain. For this formulation, a new anisotropic Finite Element (FE) method is presented, and several implementational issues are discussed.

3.1   Reparametrization

The fact that the maximal filament length varies along the lamellipodium and potentially with time has the consequence that the computational domain $B(t) = \{(\alpha, s) : 0 \le \alpha < 2\pi, \; -L(\alpha, t) \le s < 0\}$ is non-rectangular. In order to be able to use tensor product grids, we introduce the coordinate change

$$(\alpha, s, t) \rightarrow (\alpha, L(\alpha, t)s, t) \,,$$

with the new domain $(\alpha, s) \in B_0 := [0, 2\pi) \times [-1, 0)$. Accordingly, a weak formulation of the transformed version of (3), (5) is given by

$$
\begin{aligned}
0 = & \int_{B_0} \eta \left(\mu^B \partial_s^2 \mathbf{F} \cdot \partial_s^2 \mathbf{G} + L^4 \mu^A \widetilde{D_t} \mathbf{F} \cdot \mathbf{G} + L^2 \lambda_{\text{inext}} \partial_s \mathbf{F} \cdot \partial_s \mathbf{G} \right) d(\alpha, s) \\
& + \int_{B_0} \eta \eta^* \left(L^4 \widehat{\mu^S} \left(\widetilde{D_t} \mathbf{F} - \widetilde{D_t^*} \mathbf{F}^* \right) \cdot \mathbf{G} \mp L^2 \widehat{\mu^T} (\phi - \phi_0) \partial_s \mathbf{F}^\perp \cdot \partial_s \mathbf{G} \right) d(\alpha, s) \\
& - \int_{B_0} p(\rho) \left(L^3 \partial_\alpha \mathbf{F}^\perp \cdot \partial_s \mathbf{G} - \frac{1}{L} \partial_s \mathbf{F}^\perp \cdot \partial_\alpha (L^4 \mathbf{G}) \right) d(\alpha, s) \\
& + \int_0^{2\pi} \eta \left(L^2 f_{\text{tan}} \partial_s \mathbf{F} + L^3 f_{\text{inn}} \mathbf{V} \right) \cdot \mathbf{G} \Big|_{s=-1} d\alpha \mp \int_0^{2\pi} L^3 \lambda_{\text{tether}} \nu \cdot \mathbf{G} \Big|_{s=0} d\alpha \,, \quad (6)
\end{aligned}
$$

with $\mathbf{F}, \mathbf{G} \in H_\alpha^1((0, 2\pi); \; H_s^2(-1, 0))$, with the modified material derivative

$$\widetilde{D_t} = \partial_t - \left(\frac{\nu}{L} + \frac{s \partial_t L}{L} \right) \partial_s$$

and with the inextensibility constraint

$$|\partial_s \mathbf{F}(\alpha, s, t)| = L(\alpha, t) \,.$$

3.2   The Finite Element Formulation

As previously, we skip the superscripts $(\pm)$ except for those of the other family that we indicate by $*$. For $N_\alpha, N_s \in \mathbb{N}$ we define the rectangular grid

$$\alpha_i = (i-1)\Delta\alpha, \quad i = 1, \ldots, N_\alpha + 1, \qquad \Delta\alpha = \frac{2\pi}{N_\alpha},$$

$$s_j = -1 + (j-1)\Delta s, \quad j = 1, \ldots, N_s, \qquad \Delta s = \frac{1}{N_s - 1},$$

where $\alpha_{N_\alpha+1} = 2\pi$ is identified with $\alpha_1 = 0$. Then the domain $B_0 = [0, 2\pi) \times [-1, 0)$ can be decomposed into rectangular computational cells:

$$B_0 = \bigcup_{i=1}^{N_\alpha} \bigcup_{j=1}^{N_s-1} C_{i,j}, \quad \text{with } C_{i,j} = [\alpha_i, \alpha_{i+1}) \times [s_j, s_{j+1}). \tag{7}$$

We introduce the conforming Finite Element space

$$\mathscr{V} := \left\{ \mathbf{F} \in C_\alpha([0, 2\pi]; \, C_s^1([-1, 0]))^2 : \mathbf{F} \big|_{C_{i,j}} (\cdot, s) \in \mathbb{P}_\alpha^1, \right.$$

$$\left. \mathbf{F} \big|_{C_{i,j}} (\alpha, \cdot) \in \mathbb{P}_s^3 \quad \text{for } i = 1, \ldots, N_\alpha; \, j = 1, \ldots, N_s - 1 \right\},$$

of continuous functions, continuously differentiable with respect to s, and on each computational cell coinciding with a first order polynomial in α for fixed s, and a third order polynomial in s for fixed α.

For representing the elements of $\mathscr{V}$, we introduce, for $(a, s) \in C_{i,j}$, the *shape functions*

$$
\begin{aligned}
L_1^{i,j}(\alpha) &= \tfrac{\alpha_{i+1}-\alpha}{\Delta\alpha}, & G_1^{i,j}(s) &= 1 - \tfrac{3(s-s_j)^2}{\Delta s^2} + \tfrac{2(s-s_j)^3}{\Delta s^3}, \\
L_2^{i,j}(\alpha) &= 1 - L_1^{i,j}(\alpha), & G_2^{i,j}(s) &= s - s_j - \tfrac{2(s-s_j)^2}{\Delta s} + \tfrac{(s-s_j)^3}{\Delta s^2}, \\
& & G_3^{i,j}(s) &= 1 - G_1^{i,j}(s), \\
& & G_4^{i,j}(s) &= -G_2^{i,j}(s_j + s_{j+1} - s),
\end{aligned}
\tag{8}
$$

which satisfy

$$
\begin{aligned}
L_1^{i,j}(\alpha_i) &= 1, & L_1^{i,j}(\alpha_{i+1}) &= 0, \\
L_2^{i,j}(\alpha_i) &= 0, & L_2^{i,j}(\alpha_{i+1}) &= 1, \\
G_1^{i,j}(s_j) &= 1, & G_1^{i,j}(s_{j+1}) &= 0, & (G_1^{i,j})'(s_j) &= 0, & (G_1^{i,j})'(s_{j+1}) &= 0, \\
G_2^{i,j}(s_j) &= 0, & G_2^{i,j}(s_{j+1}) &= 0, & (G_2^{i,j})'(s_j) &= 1, & (G_2^{i,j})'(s_{j+1}) &= 0, \\
G_3^{i,j}(s_j) &= 0, & G_3^{i,j}(s_{j+1}) &= 1, & (G_3^{i,j})'(s_j) &= 0, & (G_{i,j})'(s_{j+1}) &= 0, \\
G_4^{i,j}(s_j) &= 0, & G_4^{i,j}(s_{j+1}) &= 0, & (G_4^{i,j})'(s_j) &= 0, & (G_4^{i,j})'(s_{j+1}) &= 1,
\end{aligned}
\tag{9}
$$

and that they span $\mathbb{P}_\alpha^1$ and, respectively, $\mathbb{P}_s^3$. Consequentially, we define the composite *Lagrange–Hermite shape functions* (see also [3]), for $(\alpha, s) \in C_{i,j}$, by

(a) H_1^C (b) H_2^C (c) H_3^C (d) H_4^C
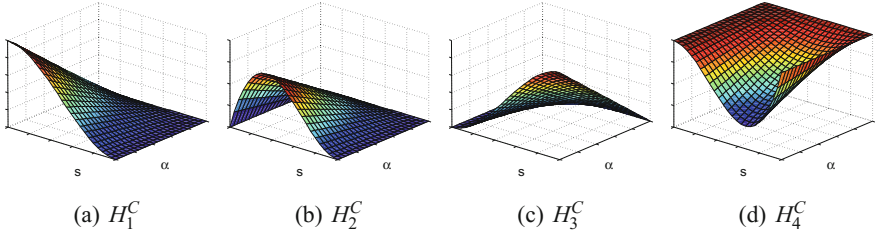
Fig. 3 Graphical representation of the Lagrange–Hermite shape functions (10). Each one of the shape functions attains the value 1 in one degree of freedom, and 0 on all the rest

$$
\begin{aligned}
H_1^{i,j}(\alpha, s) &= L_1^{i,j}(\alpha)G_1^{i,j}(s), & H_5^{i,j}(\alpha, s) &= L_2^{i,j}(\alpha)G_1^{i,j}(s), \\
H_2^{i,j}(\alpha, s) &= L_1^{i,j}(\alpha)G_2^{i,j}(s), & H_6^{i,j}(\alpha, s) &= L_2^{i,j}(\alpha)G_2^{i,j}(s), \\
H_3^{i,j}(\alpha, s) &= L_1^{i,j}(\alpha)G_3^{i,j}(s), & H_7^{i,j}(\alpha, s) &= L_2^{i,j}(\alpha)G_3^{i,j}(s), \\
H_4^{i,j}(\alpha, s) &= L_1^{i,j}(\alpha)G_4^{i,j}(s), & H_8^{i,j}(\alpha, s) &= L_2^{i,j}(\alpha)G_4^{i,j}(s),
\end{aligned}
\tag{10}
$$

and by $H_k^{i,j}(\alpha, s) = 0, k = 1, \ldots, 8$, for $(\alpha, s) \notin C_{i,j}$. Refer to Fig. 3 for a graphical representation presentation of (10). For a scalar function, there are eight degrees of freedom on each computational cell, which can be chosen as the function values and the derivatives with respect to s at the vertices. These degrees of freedom are the coefficients in a representation in terms of the basis $\{H_1^{i,j}, \ldots, H_8^{i,j}\}$.

Consequentially, every element $\mathbf{F}$ of the Finite Element space $\mathcal{V}$ can be represented in terms of the function values $\mathbf{F}_{i,j}$ and the s-derivatives $\partial_s \mathbf{F}_{i,j}$ at all grid points:

$$
\mathbf{F}(\alpha, s) = \sum_{i=1}^{N_\alpha} \sum_{j=1}^{N_s} \left(\mathbf{F}_{i,j} \Phi_{i,j}(\alpha, s) + \partial_s \mathbf{F}_{i,j} \Psi_{i,j}(\alpha, s) \right),
\tag{11}
$$

with the basis functions

$$
\begin{aligned}
\Phi_{i,j} &:= H_7^{i-1,j-1} + H_5^{i-1,j} + H_3^{i,j-1} + H_1^{i,j}, \\
\Psi_{i,j} &:= H_8^{i-1,j-1} + H_6^{i-1,j} + H_4^{i,j-1} + H_2^{i,j}, \\
& \quad i = 1, \ldots, N_\alpha, \ j = 1, \ldots, N_s.
\end{aligned}
\tag{12}
$$

The Finite Element formulation of the lamellipodium problem on the time interval $[0, T]$ is to find $\mathbf{F} \in C^1([0, T]; \mathcal{V})$, such that the weak formulation (6) holds for all $\mathbf{G} \in C([0, T]; \mathcal{V})$.

3.3   Time Discretization – Implementation Issues

In this section we go through all the terms in (6) and discuss their time discretization and some implementation details. This will lead to a semi-implicit time discretization of the problem, where at each time step a linear system has to be solved. We shall use the superscripts n and $n+1$ for the numerical approximations at the old time t_n and, respectively, the new time $t_{n+1} = t_n + \Delta t$, i.e.

$$\mathbf{F}^n(\alpha, s) = \sum_{i=1}^{N_\alpha} \sum_{j=1}^{N_s} \left(\mathbf{F}^n_{i,j} \Phi_{i,j}(\alpha, s) + \partial_s \mathbf{F}^n_{i,j} \Psi_{i,j}(\alpha, s) \right). \tag{13}$$

Finally, we shall also describe a regridding procedure in the α-direction, which has the goal to equidistribute the computational filaments.

Resistance Against Filament Bending

The bending term is evaluated at the new time step and therefore becomes

$$\int_{B_0} \eta \mu^B \partial_s^2 \mathbf{F}^{n+1} \cdot \partial_s^2 \mathbf{G} \, d(\alpha, s) \,,$$

where for $\mathbf{G}$ the basis functions (12) are inserted. For the computation of the integral, a piecewise constant approximation for η is used.

Adhesion with the Substrate

For the transport operator $\widetilde{D_t}\mathbf{F}$ in

$$\int_{B_0} \eta L^4 \mu^A \widetilde{D_t}\mathbf{F} \cdot \mathbf{G} \, d(\alpha, s) \,,$$

an explicit time discretization is used, i.e., it is replaced by

$$\frac{\mathbf{F}^{n+1} - \mathbf{F}^n}{\Delta t} - \left(\frac{v}{L} + \frac{s \partial_t L}{L} \right) \partial_s \mathbf{F}^n \,.$$

For the computation of the integral, piecewise constant approximations for η and $1/L$ were used. For the factor L^4, L was approximated by piecewise linear functions.

Stretching of Cross-Links

The friction term caused by the stretching of cross-links requires the computation of the relative velocity $D_t \mathbf{F} - D_t^* \mathbf{F}^*$, which is a subtle issue since the material derivative of $\mathbf{F}^*$ has to be evaluated at (α^*, s^*), defined by

$$\mathbf{F}(\alpha, s, t) = \mathbf{F}^*(\alpha^*, s^*, t) \,. \tag{14}$$

The computation

$$\Delta t \left(D_t \mathbf{F}(\alpha, s) - D_t \mathbf{F}^*(\alpha^*, s^*) \right)$$
$$\approx \mathbf{F}^{n+1}(\alpha, s) - \mathbf{F}^n(\alpha, s) - v \Delta t \partial_s \mathbf{F}^n(\alpha, s)$$
$$- \mathbf{F}^{n+1,*}(\alpha^*, s^*) + \mathbf{F}^{n,*}(\alpha^*, s^*) + v^* \Delta t \partial_s \mathbf{F}^{n,*}(\alpha^*, s^*)$$
$$\approx \mathbf{F}^{n+1}(\alpha, s) - \mathbf{F}^n(\alpha, s + v \Delta t) - \mathbf{F}^{n+1,*}(\alpha^*, s^*) + \mathbf{F}^{n,*}(\alpha^*, s^* + v^* \Delta t)$$

shows that it is convenient to introduce an additional $O(\Delta t)$-discretization error, replacing (14) by

$$\mathbf{F}^n(\alpha, s + v \Delta t) = \mathbf{F}^{*,n}(\alpha^*, s^* + v^* \Delta t) . \tag{15}$$

Another difficulty originates from the fact that the s^*-direction in the (α^*, s^*)-plane does not correspond to the s-direction in the (α, s)-plane, and therefore it is difficult to express the information encoded in the values of $\partial_{s^*} \mathbf{F}^*$ in terms of (α, s). We therefore decided for approximations of the cross-link terms only in terms of the filament positions:

$$\mathbf{F}^n(\alpha, s) = \sum_{i=1}^{N_\alpha} \sum_{j=1}^{N_s} \mathbf{F}_{i,j}^n \widehat{\Phi_{i,j}}(\alpha, s) , \qquad \mathbf{F}^{*,n}(\alpha^*, s^*) = \sum_{i=1}^{N_\alpha} \sum_{j=1}^{N_s} \mathbf{F}_{i,j}^{*,n} \widehat{\Phi_{i,j}}(\alpha^*, s^*) ,$$

where the hat-functions $\widehat{\Phi_{i,j}}$ are piecewise bilinear. The Eq. (15) is solved for $(\alpha, s) = (\alpha_i, s_j)$, $i = 1, \ldots, N_\alpha$, $j = 1, \ldots, N_s$, using these representations, which involves a search for the quadrilateral of $\mathbf{F}^{*,n}$-positions containing $\mathbf{F}^n(\alpha_i, s_j + v \Delta t)$. The nonlinear system is then solved by using a bilinear representation of $\mathbf{F}$, which allows to solve the system exactly. The resulting values for (α^*, s^*) are denoted by $(\alpha_{i,j}^*, s_{i,j}^*)$. Finally, the relative velocity is approximated by

$$(D_t \mathbf{F} - D_t^* \mathbf{F}^*)(\alpha, s) \approx \sum_{i=1}^{N_\alpha} \sum_{j=1}^{N_s} \frac{\mathbf{F}_{i,j}^{n+1} - \mathbf{F}^{*,n+1}(\alpha_{i,j}^*, s_{i,j}^*)}{\Delta t} \widehat{\Phi_{i,j}}(\alpha, s)$$

in the cross-link stretching term

$$\int_{B_0} \eta \eta^* L^4 \widehat{\mu^S} \left(D_t \mathbf{F} - D_t^* \mathbf{F}^* \right) \cdot \mathbf{G} \, d(\alpha, s) , \tag{16}$$

where, again η and η^* are approximated as piecewise constant and L as piecewise linear.

Twisting of Cross-Links

For the cross-link twisting term, a semi-implicit time discretization is used. The angle between filaments is evaluated at each grid point and at the old time step:

$$\phi_{i,j}^n = \arccos\left(\partial_s \mathbf{F}_{i,j}^n \cdot \partial_s \mathbf{F}^{*,n}(\alpha_{i,j}^*, s_{i,j}^*)\right) ,$$

with $(\alpha_{i,j}^*, s_{i,j}^*)$ computed as above. A piecewise constant approximation ϕ^n is then obtained from averaging over grid cells. This is used in the evaluation of

$$\int_{B_0} \eta\eta^* L^2 \widehat{\mu^T} (\phi^n - \phi_0)\partial_s \mathbf{F}^{n+1,\perp} \cdot \partial_s \mathbf{G} \, d(\alpha, s) ,$$

where also η and η^* are approximated by piecewise constant functions and L by piecewise linear functions.

Filament Repulsion

For the pressure $p(\rho)$ with $\rho = \eta/|\partial_s \mathbf{F} \cdot \partial_\alpha \mathbf{F}^\perp|$ a piecewise constant approximation ρ^n evaluated at the old time step is used. It is calculated using the representation of F given in (13) to compute cell averages of $\partial_s F$ and $\partial_\alpha F$. The function η is approximated by a piecewise constant function. The pressure term is discretized semi-implicitly as

$$\int_{B_0} p(\rho^n) \left(L^3 \partial_\alpha \mathbf{F}^{n+1,\perp} \cdot \partial_s \mathbf{G} - \frac{1}{L}\partial_s \mathbf{F}^{n+1,\perp} \cdot \partial_\alpha (L^4 \mathbf{G})\right) d(\alpha, s) .$$

As above L is approximated by a piecewise linear function, with the exception of the coefficient $1/L$, which is approximated by a piecewise constant function.

Inextensibility Constraint

With a penalization approach, the inextensibility term

$$\int_{B_0} \eta L^2 \lambda_{\text{inext}} \partial_s \mathbf{F} \cdot \partial_s \mathbf{G} \, d(\alpha, s)$$

in (6) is replaced by

$$\int_{B_0} \eta L^2 \frac{|\partial_s \mathbf{F}|^2 - L^2}{\varepsilon} \partial_s \mathbf{F} \cdot \partial_s \mathbf{G} \, d(\alpha, s) ,$$

with a small positive parameter ε. We use the semi-implicit linearization

$$\left(|\partial_s \mathbf{F}|^2 - L^2\right) \partial_s \mathbf{F} \approx \left(|\partial_s \mathbf{F}^n|^2 - L^2\right) \partial_s \mathbf{F}^{n+1} + 2\left(\partial_s \mathbf{F}^n \cdot \partial_s \mathbf{F}^{n+1} - |\partial_s \mathbf{F}^n|^2\right) \partial_s \mathbf{F}^n$$

and employ the augmented Lagrangian method, whence the inextensibility term becomes

$$\int_{B_0} \eta L^2 \left(\left(\lambda^n + \frac{|\partial_s \mathbf{F}^n|^2 - L^2}{\varepsilon}\right) \partial_s \mathbf{F}^{n+1} + \frac{2}{\varepsilon}\left(\partial_s \mathbf{F}^n \cdot \partial_s \mathbf{F}^{n+1} - |\partial_s \mathbf{F}^n|^2\right) \partial_s \mathbf{F}^n\right)$$
$$\cdot \partial_s \mathbf{G} \, d(\alpha, s) .$$

After the time step is carried out, the Lagrange multiplier is updated by

$$\lambda^{n+1} = \lambda^n + \frac{|\partial_s \mathbf{F}^n|^2 - L^2}{\varepsilon} + \frac{2}{\varepsilon} \left(\partial_s \mathbf{F}^n \cdot \partial_s \mathbf{F}^{n+1} - |\partial_s \mathbf{F}^n|^2 \right) .$$

Again, L is approximated as piecewise linear.

Spatial Equidistribution of Computational Filaments

In some simulations, the computational filaments tend to be distributed unevenly. This is avoided by a regridding procedure, where the computational barbed ends are evenly distributed along the leading edge, which can be achieved by a coordinate change $\alpha \to \beta$, defined by

$$\beta = 2\pi \int_0^\alpha |\partial_\alpha \mathbf{F}(\hat{\alpha}, 0, t)| d\hat{\alpha} \left(\int_0^{2\pi} |\partial_\alpha \mathbf{F}(\hat{\alpha}, 0, t)| d\hat{\alpha} \right)^{-1} .$$

Numerically this is realized after carrying out a time step $t_{n-1} \to t_n$, by defining a piecewise linear function $g(\alpha)$ through its values at the grid:

$$g(\alpha_i) := 2\pi \sum_{j=1}^{i-1} |\mathbf{F}_{j+1,N_s}^n - \mathbf{F}_{j,N_s}^n| \left(\sum_{j=1}^{N_\alpha} |\mathbf{F}_{j+1,N_s}^n - \mathbf{F}_{j,N_s}^n| \right)^{-1} , \quad i = 1, \ldots, N_\alpha + 1 .$$

Then $\widetilde{\alpha}_1, \ldots, \widetilde{\alpha}_{N_a+1}$ are determined as the solutions of

$$g(\widetilde{\alpha}_i) = (i - 1)\Delta\alpha , \quad i = 1, \ldots, N_\alpha + 1 .$$

Now the computational filaments, corresponding to $\alpha = \alpha_1, \ldots, \alpha_{N_\alpha+1}$, are replaced by those located at $\alpha = \widetilde{\alpha}_1, \ldots, \widetilde{\alpha}_{N_\alpha+1}$:

$$\widetilde{\mathbf{F}}_{i,j}^n := \mathbf{F}^n(\widetilde{\alpha}_i, s_j) , \qquad \widetilde{\partial_s \mathbf{F}}_{i,j}^n := \partial_s \mathbf{F}^n(\widetilde{\alpha}_i, s_j) ,$$

and the density also needs to be redefined:

$$\widetilde{\eta}_{i,j}^n := \frac{\eta^n(\widetilde{\alpha}_i, s_j)}{g'(\widetilde{\alpha}_i)} .$$

This procedure can be carried out whenever needed. In the simulations of the following section, it was done after every time step.

4 Numerical Simulations

The purpose of this section is to demonstrate that the model is capable of predicting the outcome of migration experiments on inhomogeneous adhesive patterns. In [12] the effect of varying different model parameters has been demonstrated. Additionally the model has been used to simulate chemotactic migration and to study the

effect of changes in the signaling cascade on cell shape and filament density. Here we go a step further and simulate how the shape of a migrating cell is influenced by inhomogeneous adhesive patterns. Such studies are used to better understand the interplay between adhesion, contraction, actin polymerization and other actin associated proteins.

4.1 Experiment 1: Strongly Versus Weakly Adhesive Stripes

We show that model predictions are consistent with experimental data on migration experiments published in [4]. In these experiments migrating fish keratocytes were placed on substrates coated with distinct patterns of the extra-cellular-matrix (ECM) protein fibronectin which binds to integrin transmembrane receptors mediating adhesion. In [4] striped patterns were used featuring adhesive (fibronectin containing) strips of 5 μm width and nonadhesive strips (without fibronectin) varying between 5 and 30 μm in width. In [4] it was reported that this affects cell shape in a very distinct way. Protruding bumps on the adhesive strips and lagging bumps on the nonadhesive stripes were observed and their width was correlated to the stripe width. Also it was observed that cells tend to assume a symmetric shape such that they had an equal
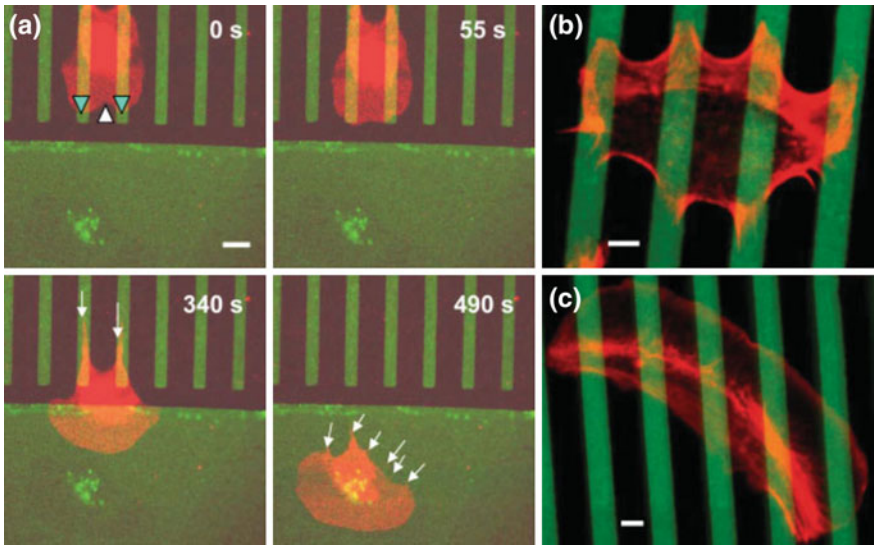

Fig. 4 Figure reproduced from [4]: "Reversible deformation of the leading edge on line patterns. **a**: ... keratocyte crawling from a 5–9 pattern ... onto an unpatterned region ... **b**: Deformation of the leading edge on a 5–7 pattern with protruding bumps on adhesive stripes and lagging bumps on non-adhesive stripes... **c**: Control experiment on a 5–7 line pattern where unprinted regions (black) are not backfilled ... rendering the substrate homogeneously adhesive. Cells restore their characteristic crescent-shaped outline ... Scale bars: 5 μm"
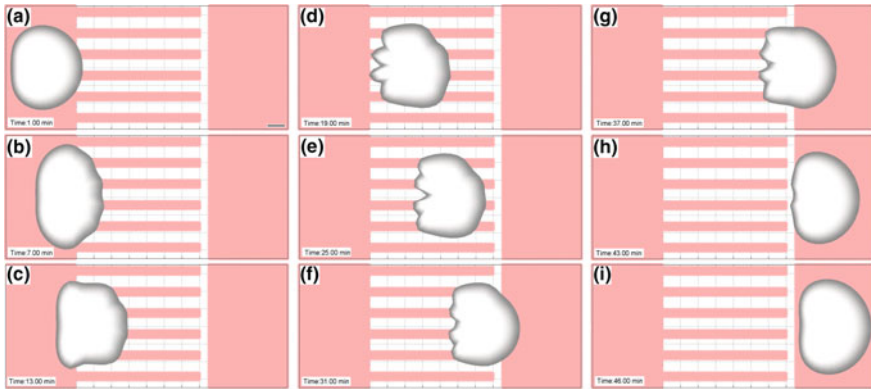
Fig. 5 a–i Times series of the simulation of a cell moving over a striped adhesive pattern (*red*) with a 80% drop in adhesiveness (*white*) between adhesive strips. *Shading* represents actin network density. Parameter values as in Table 1. The *bar* represents 10 μm

number of adhesive strips to the right and to the left of their cell center (Fig. 4 shows some of the data published in [4]).

In the numerical experiment we used the same geometrical pattern with adhesive strips of 5 μm width interspaced with 7 μm wide strips of reduced adhesiveness. In the mathematical model adhesion forces result in friction between the cell and the substrate and, speaking in numerical terms, they link one time step to the next. We simulated the inhomogeneous adhesive pattern by decreasing the friction coefficient by 80–90% in those regions of low fibronectin concentration as compared to adhesive regions. Whilst the keratocytes in the original experiments move spontaneously without an external signal, we simulate chemotactic cells under an external cue, since at this point the model cannot describe the dynamics of contractile rear bundles which stabilize autonomously migrating keratocytes. However the numerical results show that there are many similarities as far as general behavior and morphology are concerned, suggesting that the underlying phenomena are very similar. In Fig. 5a–i a time series resulting from the simulation of a cell on a striped adhesive pattern with a drop in adhesiveness of 80% is depicted. The following agreements between the simulation and the experiments (Fig. 4) were found:

- On the striped adhesion pattern the cell shape becomes more rectangular as compared to the crescent shape in the homogeneously adhesive region.
- Cells show protruding bumps on the adhesive stripes and lagging bumps on non-adhesive stripes.
- The width of the bumps is correlated with the widths of the stripes.
- Spikes appear at the rear of the cell.
- After leaving the striped region the cell resumes its crescent shape and continues to migrate as before.
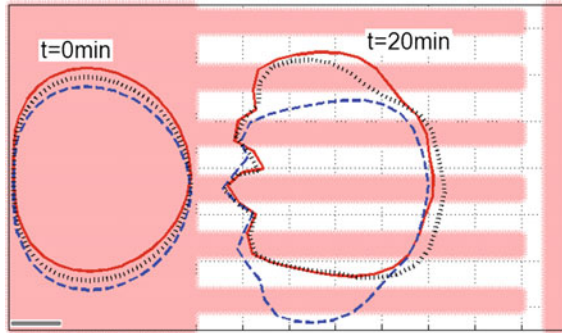
Fig. 6 Comparison of the cell shape for three different starting positions. Parameter values as in Table 1. The bar represents $10\,\mu m$
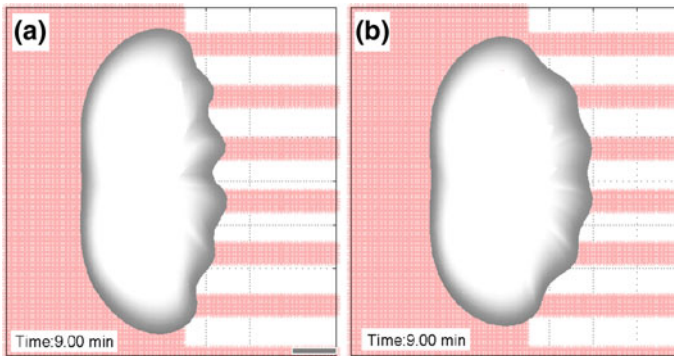

Fig. 7 Movement of a cell on an adhesive substrate (*red*) with less-adhesive stripes (*white*). *Shading* represents actin network density. **a** 90% drop in adhesiveness, **b** 80% drop in adhesiveness. Parameter values as in Table 1. The *bar* represents $10\,\mu m$

To compare the influence of the starting position on the shape of the cell, the simulation was performed with three different initial conditions differing by $2\,\mu m$ shifts in the y-direction. The outcome is depicted in Fig. 6. It can be observed that the shape of the cell starting at the lowest position (blue, dashed) differs significantly from the other two. This is due to the fact that it interacts with the lowest adhesive stripe causing it to shift further down as compared to the other cells.

In Fig. 7a, b a comparison between the bumps on stripes with a 90% (a) and a 80% (b) drop in adhesiveness is shown. Here the α-discretization used was twice as fine to resolve more details. As expected bumps when adhesiveness drops by 90% are more pronounced. Over a time interval of several minutes the amplitude of the bumps fluctuated, an observation also made in the experiment of [4].
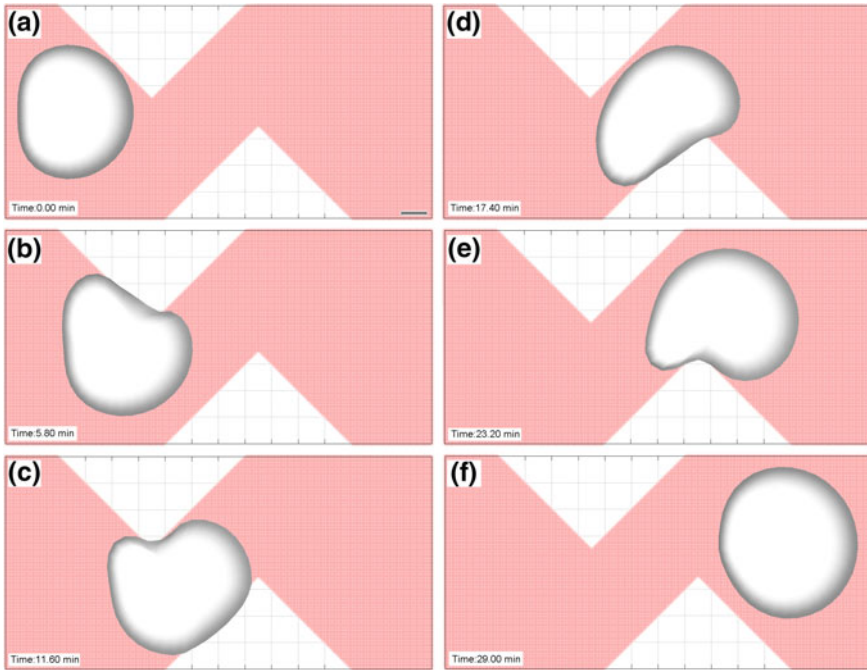
Fig. 8 Movement of a cell on an adhesive substrate (*red*) with less-adhesive spikes (*white*). *Shading* represents actin network density. Parameter values as in Table 1. The *bar* represents 10 μm

4.2 Experiment 2: Less-Adhesive Spikes on Strongly Adhesive Ground

Next we demonstrate the predictive capacity of the model simulating cell migration along an adhesive path lined by irregular regions of low adhesion. The low-adhesion pattern consists of two shifted spikes lining the trajectory of the cell from both sides. The drop in adhesiveness was chosen to be 80%. As opposed to the situation above, the cell is now able to almost fully avoid the less-adhesive regions. The behavior observed over a time period of 30 min is depicted in the time series shown in Fig. 8. The outcome of the simulation is counterintuitive in the cell does not simply slide of the nonadhesive areas. Instead it behaves as if the less-adhesive spikes were obstacles and only a very small portion of the lamellipodium enters the less-adhesive areas.

4.3 Parameters Values

For the discretization we used a time step of 0.12 s and nine nodes per filament. For the first experiment we used 36 and 72 discrete filaments, for the second one 36.

Table 1 Parameter values

Var.	Meaning	Value	Comment
μ^B	Bending elasticity	$0.07\,\mathrm{pN}\,\mu\mathrm{m}^2$	[5]
μ^A	Macroscopic friction caused by adhesions	$0.041, 0.082,$ $0.41\,\mathrm{pN}\,\mathrm{min}\,\mu\mathrm{m}^{-2}$	Lower values for less-adhesive regions, highest value for adhesive regions, order of magnitude from measurements in [10, 16], estimation and calculations in [17, 18, 20]
κ_{br}	Branching rate	$10\,\mathrm{min}^{-1}$	Order of magnitude from [7], chosen to fit $2\overline{\rho}_{\mathrm{ref}} = 90\,\mu\mathrm{m}^{-1}$ [26]
κ_{cap}	Capping rate	$5\,\mathrm{min}^{-1}$	Order of magnitude from [7], chosen to fit $2\overline{\rho}_{\mathrm{ref}} = 90\,\mu\mathrm{m}^{-1}$ [26]
c_{rec}	Arp2/3 recruitment	$900\,\mu\mathrm{m}^{-1}\,\mathrm{min}^{-1}$	Chosen to fit $2\overline{\rho}_{\mathrm{ref}} = 90\,\mu\mathrm{m}^{-1}$ [26]
κ_{sev}	Severing rate	$0.38\,\mathrm{min}^{-1}\,\mu\mathrm{m}^{-1}$	Chosen to give lamellipodium widths similar as described in [26]
μ^{IP}	Actin–myosin interaction strength	$0.1\,\mathrm{pN}\,\mu\mathrm{m}^{-2}$	
A_0	Equilibrium inner area	$450\,\mu\mathrm{m}^2$	Order of magnitude as in [25, 27]
$v_{\min}$	Minimal polymerization speed	$1.5\,\mu\mathrm{m}\,\mathrm{min}^{-1}$	In biological range
$v_{\max}$	Maximal polymerization speed	$8\,\mu\mathrm{m}\,\mathrm{min}^{-1}$	In biological range
μ^P	Pressure constant	$0.05\,\mathrm{pN}\,\mu\mathrm{m}$	
μ^S	Cross-link stretching constant	$7.1\times 10^{-3}\,\mathrm{pN}\,\mathrm{min}\,\mu\mathrm{m}^{-1}$	
μ^T	Cross-link twisting constant	$7.1 \times 10^{-3}\,\mu\mathrm{m}$	
κ_{ref}	Reference leading edge curvature for polymerization speed reduction	$(5\,\mu\mathrm{m})^{-1}$	

For the biological parameters, we used the same as those in [12], apart from the adhesion coefficient which was increased for the adhesive regions and decreased for the less-adhesive regions. They are summarized in Table 1.

References

1. W. Alt and M. Dembo. Cytoplasm dynamics and cell motion: Two-phase flow models. *Math. Biosci.*, 156(1–2):207–228, 1999.
2. L. Blanchoin, R. Boujemaa-Paterski, C. Sykes, and J. Plastino. Actin dynamics, architecture, and mechanics in cell motility. *Physiological Reviews.*
3. D. Braess. *Finite Elements. Theory, fast solvers, and applications to solid mechanics.* Cambridge University Press, 2001.
4. G. Csucs, K. Quirin, and G. Danuser. Locomotion of fish epidermal keratocytes on spatially selective adhesion patterns. *Cell Motility and the Cytoskeleton*, 64(11):856–867, 2007.
5. F. Gittes, B. Mickey, J. Nettleton, and J. Howard. Flexural rigidity of microtubules and actin filaments measured from thermal fluctuations in shape. *The Journal of Cell Biology*, 120(4):923–34, 1993.
6. M.E. Gracheva and H.G. Othmer. A continuum model of motility in ameboid cells. *Bull. Math. Biol.*, 66(1):167–193, 2004.
7. H.P. Grimm, A.B. Verkhovsky, A. Mogilner, and J.-J. Meister. Analysis of actin dynamics at the leading edge of crawling cells: implications for the shape of keratocytes. *European Biophysics Journal*, 32:563–577, 2003.
8. C.I. Lacayo, Z. Pincus, M.M. VanDuijn, C.A. Wilson, D.A. Fletcher, F.B. Gertler, A. Mogilner, and J.A. Theriot. Emergence of large-scale cell morphology and movement from local actin filament growth dynamics. 2007.
9. T. Lämmermann, M. Sixt, Mechanical modes of amoeboid cell migration. *Current Opinion in Cell Biology* **21**(5), 636–644 (2009)
10. F. Li, S.D. Redick, H.P. Erickson, and V.T. Moy. Force measurements of the $\alpha 5\beta 1$ integrin-fibronectin interaction. *Biophysical Journal*, 84(2):1252–1262, 2003.
11. I.V. Maly and G.G. Borisy. Self-organization of a propulsive actin network as an evolutionary process. *Proc. Natl. Acad. Sci.*, 98:11324–11329, 2001.
12. A. Manhart, D. Oelz, C. Schmeiser, and N. Sfakianakis. An extended Filament Based Lamellipodium Model produces various moving cell shapes in the presence of chemotactic signals. *J. Theor. Biol.*, 382:244–258, 2015.
13. A. F. M. Marée, A. Jilkine, A. Dawes, V. A. Grieneisen, and L. Edelstein-Keshet. Polarization and movement of keratocytes: a multiscale modelling approach. *Bull. Math. Biol.*, 68(5):1169–1211, 2006.
14. R.W. Metzke, M.R.K. Mofrad, and W.A. Wall. Coupling atomistic simulation to a continuum based model to compute the mechanical properties of focal adhesions. *Biophysical Journal*, 96(3, Supplement 1):673a –, 2009.
15. S.J. Mousavi and M.H. Doweidar. Three-dimensional numerical model of cell morphology during migration in multi-signaling substrates. *PLoS ONE*, 10(3), 2015.
16. A.F. Oberhauser, C. Badilla-Fernandez, M. Carrion-Vazquez, and J.M. Fernandez. The mechanical hierarchies of fibronectin observed with single-molecule AFM. *Journal of Molecular Biology*, 319(2):433–47, 2002.
17. D. Oelz and C. Schmeiser. *Cell mechanics: from single scale-based models to multiscale modeling.*, chapter How do cells move? Mathematical modeling of cytoskeleton dynamics and cell migration. Chapman and Hall, 2010.
18. D. Oelz and C. Schmeiser. Derivation of a model for symmetric lamellipodia with instantaneous cross-link turnover. *Archive for Rational Mechanics and Analysis*, 198:963–980, 2010.
19. D. Oelz and C. Schmeiser. Simulation of lamellipodial fragments. *Journal of Mathematical Biology*, 64:513–528, 2012.
20. D. Oelz, C. Schmeiser, and J.V. Small. Modeling of the actin-cytoskeleton in symmetric lamellipodial fragments. *Cell Adhesion and Migration*, 2:117–126, 2008.
21. B. Rubinstein, K. Jacobson, and A. Mogilner. Multiscale two-dimensional modeling of a motile simple-shaped cell. *Multiscale Model. Simul.*, 3(2):413–439, 2005.
22. B. Rubinstein, M.F. Fournier, K. Jacobson, A.B Verkhovsky, and A. Mogilner. Actin-myosin viscoelastic flow in the keratocyte lamellipod. *Biophysical Journal*, 97(7):1853–1863, 2009.

23. Y. Sakamoto, S. Prudhomme, and M.H. Zaman. Modeling of adhesion, protrusion, and contraction coordination for cell migration simulations. *Journal of Mathematical Biology*, 68(1–2):267–302, 2014.
24. T.E. Schaus, E. W. Taylor, and G. G. Borisy. Self-organization of actin filament orientation in the dendritic-nucleation/array-treadmilling model. *Proc Natl Acad Sci USA*, 104(17):7086–91, 2007.
25. J.V. Small, G. Isenberg, and J.E. Celis. Polarity of actin at the leading edge of cultured cells. *Nature*, bf 272:638–639, 1978.
26. J.V. Small, T. Stradal, E. Vignal, and K. Rottner. The lamellipodium: where motility begins. *Trends in Cell Biology*, 12(3):112–20, 2002.
27. A.B. Verkhovsky, T.M. Svitkina, and G.G. Borisy. Self-polarisation and directional motility of cytoplasm. *Current Biology*, 9(1):11–20, 1999.
28. M. Vinzenz, M. Nemethova, F. Schur, J. Mueller, A. Narita, E. Urban, C. Winkler, C. Schmeiser, S.A. Koestler, K. Rottner, G.P. Resch, Y. Maeda, and J.V. Small. Actin branching in the initiation and maintenance of lamellipodia. *Journal of Cell Science*, 125(11):2775–2785, 2012.